

# Soft tissue 3D imaging in the lab through optimised propagation-based phase contrast computed tomography

BERIT ZELLER-PLUMHOFF<sup>1,2,\*</sup>, JOSHUA L. MEAD<sup>1</sup>, DECK TAN<sup>1</sup>, TIINA ROOSE<sup>1</sup>, GERALDINE F. CLOUGH<sup>3</sup>, RICHARD P. BOARDMAN<sup>4</sup> AND PHILIPP SCHNEIDER<sup>1,4,\*</sup>

<sup>1</sup>Bioengineering Research Group, Faculty of Engineering and the Environment, University of Southampton, Southampton, UK

<sup>2</sup>Helmholtz-Zentrum Geesthacht, Centre for Coastal and Materials Research, Geesthacht, Germany

<sup>3</sup>Institute for Health Sciences, University of Southampton, Southampton, UK

<sup>4</sup> $\mu$ -VIS X-ray Imaging Centre, Faculty of Engineering and the Environment, University of Southampton, Southampton, UK

\*[berit.zeller-plumhoff@hzg.de](mailto:berit.zeller-plumhoff@hzg.de), [p.schneider@soton.ac.uk](mailto:p.schneider@soton.ac.uk)

**Abstract:** Tomographic phase contrast imaging using hard X-rays is instrumental in revealing and understanding the three-dimensional (3D) anatomic structure of biological tissues. However, phase contrast imaging is often limited to synchrotron radiation sources to which access is limited and highly competitive. Therefore, it is critical to enable high-quality phase contrast tomography using lab-based X-ray sources. We present a lab-based soft tissue 3D imaging approach through optimised in-line phase contrast computed tomography, building upon and going beyond previous work of Bidola *et al.* [Opt Express **23**(23), 30000-30013 (2015)]. Murine soleus muscle was used as a test specimen to systemically optimise source-to-sample and sample-to-detector distances, exposure time and the critical ratio used for Paganin phase retrieval before tomographic reconstruction. Larger propagation distances combined with longer exposure times resulted in improved image quality. Whilst the contrast-to-noise ratio of lab-based phase contrast imaging was found to be lower than that of synchrotron-based imaging, important microscopic soft tissue features, such as nerves, could well be distinguished in 3D from surrounding tissue for both imaging modalities. This shows that lab-based X-ray sources present a viable alternative to synchrotron radiation sources for tomographic phase contrast imaging of soft tissues.

© 2017 Optical Society of America

**OCIS codes:** (350.5030) Phase, (110.6955) Tomographic imaging, (110.7440) X-ray imaging, (110.3000) Image quality assessment

---

## References

1. S. C. Mayo, A. W. Stevenson, and S. W. Wilkins, "In-line phase-contrast X-ray imaging and tomography for materials science," *Materials* **5**, 937-965 (2012).
  2. A. Bravin, P. Coan, and P. Suortti, "X-ray phase-contrast imaging: from pre-clinical applications towards clinics," *Phys. Med. Biol.* **58**, R1-R35 (2013).
  3. A. Nugent "Coherent methods in the X-ray sciences," *Advances in Physics* **59**, 1-99 (2010).
  4. V. V. Lider, and K. M. V, "X-ray phase-contrast methods | SpringerLink," *Crystallography Reports* **58**, 769-787 (2013).
  5. A. Olivo, and E. Castelli, "X-ray phase contrast imaging: From synchrotrons to conventional sources," *Rivista Del Nuovo Cimento* **37**, 467-508 (2014).
  6. S. W. Wilkins, Y. I. Nesterets, T. E. Gureyev, S. C. Mayo, A. Pogany, and A. W. Stevenson, "On the evolution and relative merits of hard X-ray phase-contrast imaging methods," *Philosophical Transactions of the Royal Society A* **372** (2014).
  7. D. Zhang, F. Meng, J. Rong, X. Wu, and H. Liu, "In-line Phase-sensitive X-ray Imaging," in *Advances in Medical Physics*, D. J. Godfrey, S. K. Das, and A. B. Wolbarst, eds. (Medical Physics Publishing, 2014), p. 143.
  8. M. Fratini, I. Bukreeva, G. Campi, F. Brun, G. Tromba, P. Modregger, D. Bucci, G. Battaglia, R. Spano, M. Mastrogiacomo, H. Requardt, F. Giove, A. Bravin, and A. Cedola, "Simultaneous submicrometric 3D imaging of the micro-vascular network and the neuronal system in a mouse spinal cord," *Sci Rep* **5**, 8514 (2015).
-

9. B. Zeller-Plumhoff, T. Roose, O. L. Katsamenis, M. N. Mavrogordato, C. Torrens, P. Schneider, and G. F. Clough, "Phase contrast synchrotron radiation computed tomography of muscle spindles in the mouse soleus muscle," *Journal of Anatomy* 230, 859-865 (2017).
10. S. Mohammadi, E. Larsson, F. Alves, S. Dal Monego, S. Biffi, C. Garrovo, A. Lorenzon, G. Tromba, and C. Dullin, "Quantitative evaluation of a single-distance phase-retrieval method applied on in-line phase-contrast images of a mouse lung," *Journal of Synchrotron Radiation* 21, 784-789 (2014).
11. S. A. McDonald, F. Marone, C. Hintermuller, G. Mikuljan, C. David, F. Pfeiffer, and M. Stampanoni, "Advanced phase-contrast imaging using a grating interferometer," *J Synchrotron Radiat* 16, 562-572 (2009).
12. X. Wu, A. Yan, and H. Liu, "X-ray phase-attenuation duality and phase retrieval," *Optics Letters* 30, 379-381 (2005).
13. D. Paganin, S. C. Mayo, T. E. Gureyev, P. R. Miller, and S. W. Wilkins, "Simultaneous phase and amplitude extraction from a single defocused image of a homogeneous object," *J. Microsc.-Oxford* 206, 33-40 (2002).
14. A. Pogany, D. Gao, and S. W. Wilkins, "Contrast and resolution in imaging with a microfocus x-ray source," *Review of Scientific Instruments* 68 (1997).
15. F. Pfeiffer, T. Weitkamp, O. Bunk, and C. David, "Phase retrieval and differential phase-contrast imaging with low-brilliance X-ray sources," *Nature Physics* 2, 258-261 (2006).
16. P. M. Bidola, I. Zanette, K. Achterhold, C. Holzner, and F. Pfeiffer, "Optimization of propagation-based phase-contrast imaging at a laboratory setup," *Opt Express* 23, 30000-30013 (2015).
17. F. Marone, R. Mokso, G. Mikuljan, A. Isenegger, P. Modregger, B. Pinzer, T. Thuring, K. Mader, M. S. L. S. Stampanoni, Paul Scherrer Institut, Villigen (Switzerland), U. a. E. Z. Institute for Biomedical Engineering, Zurich (Switzerland)], J. S. L. S. Fife, Paul Scherrer Institut, Villigen (Switzerland), and E. Computational Materials Laboratory, Lausanne (Switzerland)], "Present and Future X-ray Tomographic Microscopy at TOMCAT," *AIP Conference Proceedings* 1365 (2011).
18. M. Stampanoni, A. Groso, A. Isenegger, G. Mikuljan, Q. Chen, D. Meister, M. Lange, R. Betemps, S. Henein, R. Abela, J.-Y. Choi, and S. Rah, "TOMCAT: A beamline for TOMographic Microscopy and Coherent rAdiology experimenTs," *AIP Conference Proceedings* 879 (2007).
19. T. E. Gureyev, Y. I. Nesterets, A. W. Stevenson, P. R. Miller, A. Pogany, and S. W. Wilkins, "Some simple rules for contrast, signal-to-noise and resolution in in-line x-ray phase-contrast imaging," *Opt Express* 16, 3223-3241 (2008).
20. B. L. Henke, E. M. Gullikson, and J. C. Davis, "X-Ray Interactions: Photoabsorption, Scattering, Transmission, and Reflection at E = 50-30,000 eV, Z = 1-92," *Atomic Data and Nuclear Data Tables* 54, 181-342 (2017).
21. M. J. Kitchen, G. A. Buckley, T. E. Gureyev, M. J. Wallace, N. Andres-Thio, K. Uesugi, N. Yagi, S. B. Hooper, and . "CT dose reduction factors in the thousands using X-ray phase contrast," *arXiv:1704.03556v1* (2017).
22. R. Gradl, M. Dierolf, L. Hehn, B. Günther, A. Ö. Yildirim, B. Gleich, K. Achterhold, F. Pfeiffer, and K. S. Morgan, "Propagation-based phase-contrast X-ray imaging at a compact light source," *Sci Rep-Uk* 7, 4908 (2017).
23. S. C. Mayo, P. R. Miller, S. W. Wilkins, T. J. Davis, D. Gao, T. E. Gureyev, D. Paganin, D. J. Parry, A. Pogany, A. W. Stevenson "Quantitative X-ray projection microscopy: phase-contrast and multi-spectral imaging", *J Microsc* 207, 79-96 (2002).
24. R. Hofmann, J. Moosmann, T. Baumbach, "Criticality in single-distance phase retrieval", *Opt Express* 19, 25881-25890 (2011).
25. J. Moosmann, R. Hofmann, A. Bronnikov, T. Baumbach, "Nonlinear phase retrieval from single-distance radiograph", *Opt Express* 18, 25771-25785 (2010).
26. J. Moosmann, R. Hofmann, T. Baumbach, "Single-distance phase retrieval at large phase shifts", *Opt Express* 19, 12066-12073 (2011).
27. L. Turner, B. Dhal, J. Hayes, A. Mancuso, K. Nugent, D. Paterson, R. Scholten, C. Tran, A. Peele, "X-ray phase imaging: Demonstration of extended conditions for homogeneous objects", *Opt Express* 12, 2960-2965 (2004).
28. T. E. Gureyev, T. J. Davis, A. Pogany, S. C. Mayo, S. W. Wilkins, "Optical phase retrieval by use of first Born- and Rytov-type approximations", *Appl Opt* 43, 2418-2430 (2004).
29. A. Burvall, U. Lundstrom, P. A. Takman, D. H. Larsson, H. M. Hertz, "Phase retrieval in X-ray phase-contrast imaging suitable for tomography", *Opt Express* 19, 10359-10376 (2011).

---

## 1. Introduction

Three-dimensional X-ray tomographic imaging of soft tissues, such as brain, colon, lung, muscle, skin and other organs, can be used to enhance the understanding of the tissue structure and how it is linked to the tissue function in health and disease. As the image contrast of soft tissues for X-ray absorption-based tomography is intrinsically weak due to their low and rather uniform X-ray attenuation profile, which is similar to that of water, phase contrast methods are suggested as an alternative [1-6]. In particular, grating-based methods and propagation-based phase contrast imaging (PPCI) [7] have been used frequently. These approaches were used to show the nervous and vascular structures in the spinal cord [8], the nervous features in mouse muscles [9], the microstructure of mouse lung [10], and the substantia nigra of the brain [11] for instance.

PPCI draws on phase shifts of the X-ray wave induced by an object, leading to the build-up of interference patterns after a certain X-ray propagation distance, or sample-to-detector distance, and hence to the formation of intensity oscillations, delineating fringes of the object's internal and external boundaries, which can be captured by a detector. These images can then be used to separate the X-ray attenuation from X-ray phase shift induced by the object, detectable as (Fresnel) diffraction patterns in a spatially resolved manner, which are related to the local electron density. Moreover, dealing with soft tissues, which are composed primarily of light elements with low atomic numbers, Wu *et al.* observed [12] that soft tissue attenuation cross-sections for hard X-rays can be approximated by incoherent scattering that is proportional to the atomic number. Based on these observations, a complementary relationship between phase shift and X-ray attenuation for quasi-homogeneous and weakly absorbing objects, a so-called 'phase-attenuation' duality, has been suggested by the same researchers [12], stating that the linear absorption coefficient and the phase change are both proportional to the local electron density of the object, which can be exploited for phase retrieval through PPCI using a single propagation distance only [13].

However, PPCI is often restricted to synchrotron radiation sources due to the requirements of spatial coherence of the X-ray waves, yet access to (highly coherent) synchrotron sources is limited and highly competitive. Therefore, it is critical to also enable phase contrast-based tomography using lab-based X-ray sources that are (only) partially coherent. PPCI generally requires high lateral spatial coherence that is inversely related to the X-ray source size, which means that a small source size is a prerequisite for successful PPCI. On the other hand, the constraints for the longitudinal or chromatic coherence of the incident X-ray waves are more relaxed, such that polychromatic lab sources become viable for PPCI [14]. The usage of gratings to achieve phase contrast with tube X-ray sources had been reported by Pfeiffer *et al.* [15]. Furthermore, Bidola *et al.* recently showed that PPCI is possible and can be optimised to some extent using a commercial X-ray tube [16]. We believe that the study by Bidola *et al.* requires further experiments and quantitative analysis to study the impact of the X-ray exposure time on image quality, in order to optimise tomographic PPCI of soft tissues in the lab in a systematic fashion. In particular, we call into question the conclusion that phase contrast is optimised at low source-to-sample and sample-to-detector distances [16]. In addition, the sample investigated by Bidola *et al.* was an ant head [16], which is composed mainly of chitin, a substance that we would not consider a soft tissue *per se*.

In this work, we are deriving and presenting optimised experimental settings for tomographic PPCI of a soft tissue sample (mouse soleus muscle) [9] using a commercial X-ray tube. Our investigation includes the effect of adjusting the exposure time for longer propagation distances, as well as the impact of the critical  $\delta/\beta$  or  $\delta/\mu$  ratio (see Methods) chosen for Paganin phase retrieval [13]. Moreover, we are directly comparing the image quality of the PPCI data obtained using the lab-based X-ray source and using synchrotron radiation, in order to demonstrate the image quality difference one can expect.

## 2. Methods

### 2.1 Sample preparation

All animal procedures were in accordance with the regulations of the United Kingdom Animals (Scientific Procedures) Act 1986. One soleus muscle was obtained from a male C57BL/6 mouse and processed for CT imaging as described previously [9].

### 2.2 X-ray imaging

PPCI was performed using both a lab-based X-ray microscope (Versa 510; ZEISS Xradia, Pleasanton, CA, USA) at the  $\mu$ -VIS X-ray Imaging Centre of the University of Southampton and using synchrotron radiation at the TOMCAT beamline [17, 18] of the Swiss

Light Source (SLS). Imaging at TOMCAT was performed at an energy of 14 keV, a voxel size of 0.65  $\mu\text{m}$ , an exposure time of 180 ms and using 1601 projections (with additional 32 dark field and 160 flat field images), as previously described in [9]. Imaging on the lab-based X-ray microscope was performed as described by Bidola *et al.* [16]. The nominal spot size of the system has not been determined but assumed to be identical to 1.8  $\mu\text{m}$  as derived by Bidola *et al.* [16]. In particular, a peak X-ray energy of 40 keV and a tube power of 3 W were used, with binning two times on the detector, resulting in a binned voxel size of 0.96  $\mu\text{m}$  and a field of view of 0.79 mm. The source-to-sample and sample-to-detector distances were varied and the exposure time was adjusted accordingly, as described in the next subsection and summarised in Table 1. Figure 1 (a) and (b) show a sketch of the setup for lab-based PPCI and synchrotron-based PPCI, respectively. The muscle was mounted such that its longitudinal axis was parallel to the rotation axis.

### 2.3 Propagation distances

The propagation distances studied using the lab-based X-ray microscope were chosen according to Bidola *et al.* [16] (Table 1). The smallest source-to-sample distance ( $R_1$ ) and sample-to-detector distance ( $R_2$ ) were 10 and 60 mm, respectively (abbreviated as position RI<sub>Lab</sub>). For position RII<sub>Lab</sub> and RIII<sub>Lab</sub>, these distances have been both doubled and quadrupled, such that the geometric magnification ( $M = (R_1+R_2)/R_1$ ) remained constant. The effective propagation distance  $Z_{eff}$ , required for the calculation of the projected thickness  $t$  and the respective phase shift  $\varphi$  (see Appendix), is given by

$$Z_{eff} = \frac{R_1 R_2}{R_1 + R_2}. \quad (1)$$

For a sweep of propagation distances at TOMCAT,  $R_2$  was varied between 30 mm and 60 mm in steps of 10 mm, where  $Z_{eff}$  equals roughly  $R_2$  and the geometrical magnification is approximately 1 because  $R_1 \gg R_2$ .

### 2.4 Exposure times

With increasing propagation distances, the photon count captured by the detector of the lab-based X-ray microscope decreased significantly. Whilst exposing the detector at position RI<sub>Lab</sub> for 5 sec, we increased the exposure time fourfold for every doubling of the propagation distance ('adjusted') to ensure similar photon counts [19]. For comparison, we also imaged at 5 sec exposure time ('non-adjusted') for positions RII<sub>Lab</sub> and RIII<sub>Lab</sub>. Due to the parallel geometry of the X-ray beam at synchrotrons, such adjustments of exposure times were not required for the sweep of propagation distances at TOMCAT. See Table 1 for a summary of the different propagation distances and exposure times used in this study.

**Table 1. Summary of propagation distances and exposure times for PPCI**

X-ray source	Position	$R_1$ (mm)	$R_2$ (mm)	$Z_{eff}$ (mm)	Exposure time (s)
Versa 510, Zeiss Xradia	RI <sub>Lab</sub>	10	60	8.57	5.0
	RII <sub>Lab</sub>	20	120	17.14	5.0
	RII <sub>Lab</sub>	20	120	17.14	20.0
	RIII <sub>Lab</sub>	40	240	34.29	5.0
	RIII <sub>Lab</sub>	40	240	34.29	82.0
SLS, TOMCAT	RI <sub>Syn</sub>	~ 25'000	30	~29.96	0.18
	RII <sub>Syn</sub>	~ 25'000	40	~39.94	0.18

RIII <sub>Syn</sub>	~ 25'000	50	~49.90	0.18
RIV <sub>Syn</sub>	~ 25'000	60	~59.86	0.18

## 2.5 $\delta/\mu$ ratio for Paganin phase retrieval

For the calculation of the projected thickness and the related phase shift (see Appendix 5.1) a number of different ratios of the decrement of the real part of the refractive index  $\delta$  and the imaginary part of the refractive index  $\beta$  were tested.  $\beta$  is related to the linear attenuation coefficient  $\mu$  via  $\mu = 4\pi/\lambda \cdot \beta$ . The different  $\delta/\mu$  ratios were tested to determine which ratio provides the best image quality in terms of the signal-to-noise ratio (SNR) and the known trade-off for PPCI [19] between image contrast (contrast-to-noise ratio or CNR) and spatial resolution. This trade-off is a function of the inverse Fresnel number and thus, of the effective propagation distance (and X-ray wavelength and the point spread function of the imaging system) [14]. As (murine) muscle and most soft tissues consist mainly of water when fresh, the  $\delta/\mu$  ratio of water has been trialed. At the same time, since the muscle had been dehydrated and embedded in paraffin wax, by which the whole specimen was perfused, the  $\delta/\mu$  ratio for paraffin wax was also tested. The values for  $\delta$  and  $\mu$  for water and paraffin wax at an effective X-ray energy of 12.2 keV (see Appendix 5.1) were obtained from the X-ray Database from the Center for X-Ray Optics at the Lawrence Berkeley National Laboratory's Materials Sciences Division (<http://henke.lbl.gov>, accessed 27-September-2017) [20]. The material density of water and paraffin wax are tabulated in the database as 0.9 g/cm<sup>3</sup> and 2.2 g/cm<sup>3</sup>, respectively. In addition to these tabulated numbers further  $\delta/\mu$  ratios at different orders of magnitude (see Table 2 for a summary) have been selected to determine a  $\delta/\mu$  ratio for optimal image quality (see below). Tomographic data acquired at RIII<sub>Lab</sub> using an adjusted exposure time (see Table 1) has been evaluated over a large range (see below) to determine the  $\delta/\mu$  optimal ratio.

**Table 2. Summary of  $\delta/\mu$  ratios tested for phase retrieval for RIII<sub>Lab</sub>**

Test name	$\mu$ (m <sup>-1</sup> )	$\delta$	$\delta/\mu$ (m)
1	2.01E-01	1.00E-06	4.98E-06
2	7.39E-02	1.00E-07	1.35E-06
3	2.01E-01	1.00E-07	4.98E-07
4	7.39E-02	1.00E-08	1.35E-07
5	2.01E-01	1.00E-08	4.98E-08
Paraffin wax <sup>a</sup>	97.8	1.44E-06	1.47E-08
Water <sup>a</sup>	277	1.56E-06	5.63E-09
6	7.39	1.00E-08	1.35E-09
7	20.09	1.00E-08	4.98E-10
8	54.6	1.00E-08	1.83E-10
9	148.41	1.00E-08	6.74E-11
10	403.43	1.00E-08	2.48E-11

<sup>a</sup>Computed from [20] respectively <http://henke.lbl.gov> at an effective energy of 12.2 keV.

Subsequently, the optimal ratio for RI<sub>Lab</sub>, RII<sub>Lab</sub>, RI<sub>Syn</sub> and RIV<sub>Syn</sub> was determined with a sweep around the  $\delta/\mu$  ratio chosen for RIII<sub>Lab</sub>. As  $Z_{eff}(RI_{Lab}) = Z_{eff}(RIII_{Lab})/4$  it follows that if  $I/I_0$  (the intensity of the X-ray beam on the detector divided by the intensity of the incident X-ray beam) is of similar magnitude for both distances  $\delta/\mu(RI_{Lab}) = 4 \cdot \delta/\mu(RIII_{Lab})$  (see equation

(5) in Appendix 5.1). Additionally, although  $Z_{eff}(RII_{Lab}) \approx Z_{eff}(RI_{Syn})$  the detector pixel size was different (i.e. 6.72  $\mu\text{m}$  for lab-based case and 0.65  $\mu\text{m}$  for the synchrotron case) and hence, the  $\delta/\mu$  ratio requires adjustment. For the distances in-between, the ratio was determined by linear interpolation. See figures in Appendix 5.2 for the specific  $\delta/\mu$  ratios tested.

## 2.6 Paganin phase retrieval and CT reconstruction

Phase retrieval through the calculation of the projected thickness  $t$  (see Appendix 5.1) and the phase shift

$$\varphi = \frac{-2\pi\delta}{\lambda t} \quad (1)$$

has been performed using Octopus Imaging Software (Octopus Reconstruction 8.4 and 8.9; XRE NV (formerly Inside Matters), Ghent, Belgium). Paganin phase retrieval [13] was employed for the respective  $R_1$  and  $R_2$  distances using different  $\delta/\mu$  ratios (Table 2). For tomographic reconstruction of three-dimensional (3D) data from phase-retrieved two-dimensional (2D) images standard filtered backprojection using a ramp filter was applied.

## 2.7 Assessment of tomographic image quality

Tomographic image quality as a function of  $\delta/\mu$  ratio has been studied at  $RII_{Lab}$ ,  $RI_{Lab}$ ,  $RII_{Lab}$ ,  $RI_{Syn}$  and  $RIV_{Syn}$  (using the adjusted exposure time (see Table 1) for the lab-based system). Here, image quality was considered as the general strength of the tissue signal in comparison to the image noise (SNR) and the contrast of the tissue against the surrounding paraffin wax (CNR). SNR and CNR were computed as follows [10]:

$$SNR = \frac{S_{sample}}{\sigma_{background}} \quad (2)$$

and

$$CNR = \frac{S_{sample} - S_{background}}{\sqrt{0.5 \cdot (\sigma_{sample}^2 + \sigma_{background}^2)}}. \quad (3)$$

In the above equations  $S$  and  $\sigma$  denote the mean value and standard deviation of the greyscale value in the region of interest in the reconstructed tomographic image data, respectively.

In order to assess the overall SNR and CNR of a data set, the measures were computed in 300 slices around the centre slice of the image stack for lab-based PPCI and 300 slices for synchrotron-based PPCI (regions depicted in Figure 1 (c) and (d), respectively), and for 5 different regions within each slice. Figure 1 (e) and (f) depict a central slice of the muscle in which the regions were highlighted for both imaging modalities. Regions 1-5 were used to determine  $S_{sample}$  and region 6 provided the background signal and noise. Additionally, as SNR and especially CNR are not robust in cases where the images are strongly blurred ( $\sigma_{background} \rightarrow 0$  and  $(S_{Sample} - S_{background}) \rightarrow 0$ ) and structural details lost, the quality of the images was also assessed visually to decide if an image had become too blurred so that soft tissue features could not be distinguished.

To characterise sharpness and hence determine the influence of the experimental settings on spatial resolution, line profiles (LPs) have been created over a feature in the sample with well-defined edges (region ‘LP’ in Figure 1 (e) and (f)). Several line profiles within region ‘LP’ were recorded perpendicular and across the edge, and averaged to give a mean edge response profile. Using line profiles, we could examine whether any (unwanted) fringes (due to X-ray interference) at feature boundaries in the tomographic PPCI data was visible or

whether the image was smoothed too strongly (lost image sharpness) by the applied Paganin filter, making it difficult to differentiate between the muscle tissue and the background.

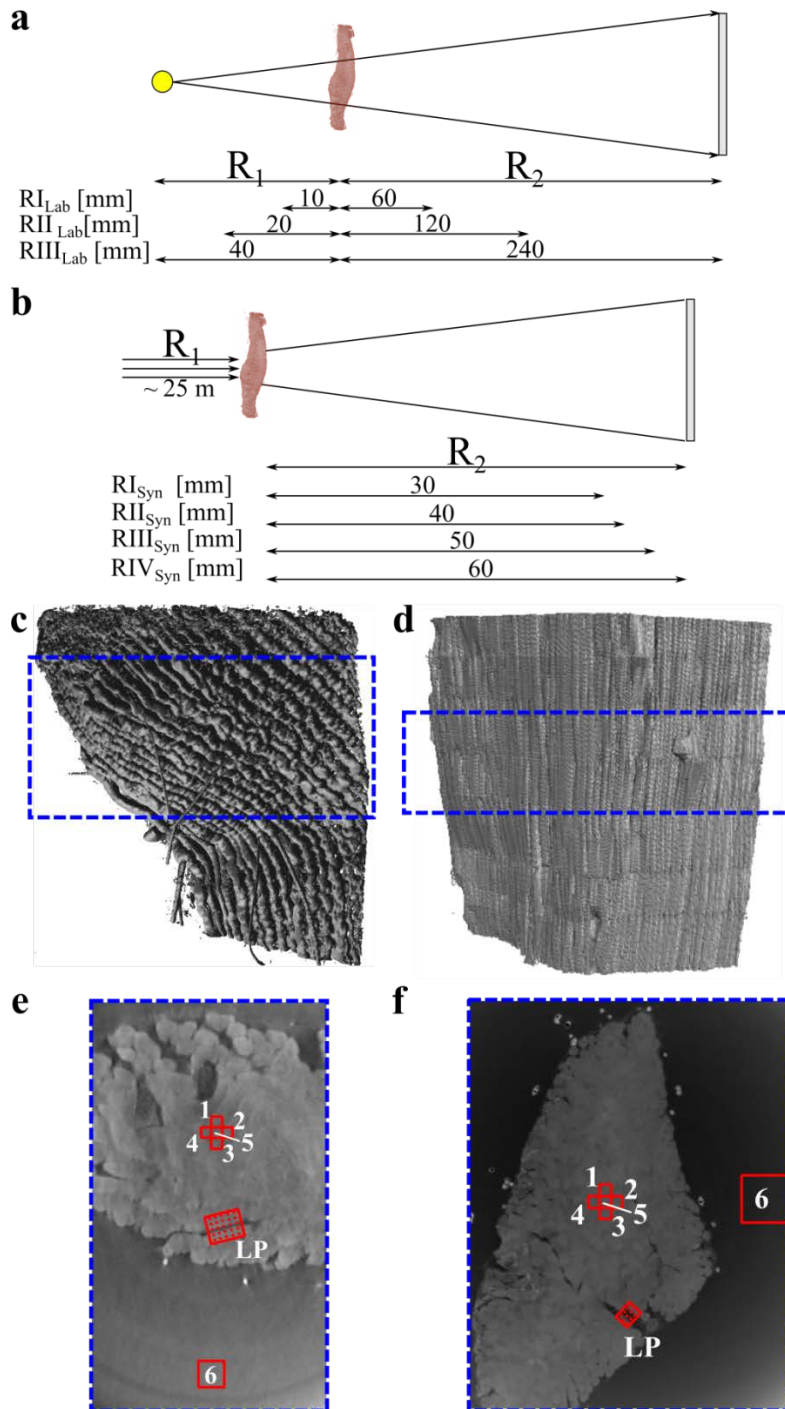


Fig. 1. Comparison of lab-based and synchrotron radiation-based PPCI setup. (a) & (b) Source-to-object and sample-to-detector distances in lab-based and synchrotron setup, respectively. (c) & (d) Isosurface renderings of the imaged part of the muscle for lab-based and synchrotron case, respectively, with regions of interest indicated by blue boxes, which were used for computation of the signal-to-noise and contrast-to-noise ratio levels. (e) & (f) Reconstructed

tomographic slices through a central plane of the muscle for lab-based and synchrotron case, respectively, depicting regions 1-6 used to compute the signal-to-noise and contrast-to-noise ratio and the region (labelled 'LP') in which line profiles were recorded.

### 3. Results

#### 3.1 Image quality and $\delta/\mu$ ratio

The image quality resulting from phase retrieval with different  $\delta/\mu$  ratios was firstly characterised using SNR and CNR (Fig. 2 (a)) and by parallel visual assessment of the respective reconstructed tomographic data sets.

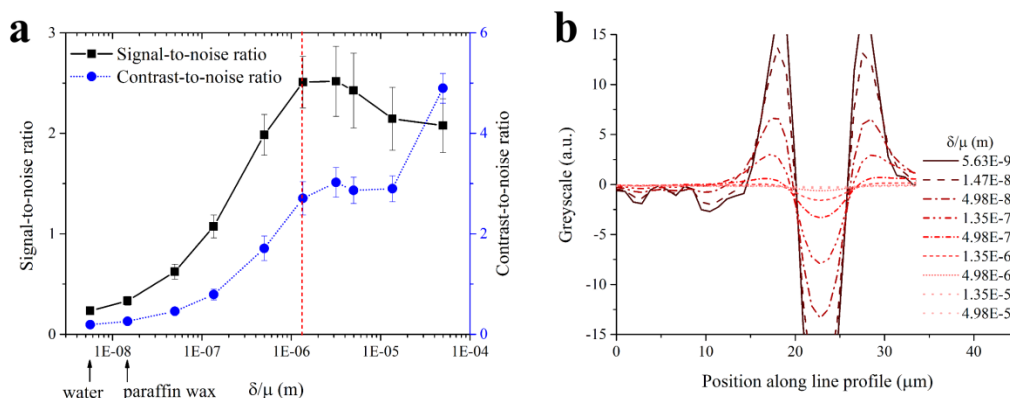


Fig. 2. Image quality from PPCI on a lab-based X-ray microscope for different  $\delta/\mu$  ratios. (a) Signal-to-noise ratio or SNR (black solid line) and contrast-to-noise ratio or CNR (blue dashed line) and (b) line profiles over two feature boundaries for varying  $\delta/\mu$  ratios at position  $R_{III,lab}$  and adjusted exposure time on a lab-based X-ray microscope.  $\delta/\mu$  ratios for paraffin wax and water resulted in low SNR and CNR ratios. Small  $\delta/\mu$  ratios led to enhanced feature boundaries within tomographic reconstructions, whilst larger  $\delta/\mu$  ratios resulted in strong smoothing of feature boundaries. The optimum ratio  $\delta/\mu$  was thus identified in-between those extremes, in the range of  $4.98 \times 10^{-6}$  m and  $4.98 \times 10^{-7}$  m. The selected value of  $1.35 \times 10^{-6}$  m for  $\delta/\mu$  is highlighted by the vertical red dotted line in (a).

The image quality results presented in Figure 2 (a) suggest that for PPCI on the lab-based X-ray microscope the mean stack SNR increased up to  $\delta/\mu = 1.35 \times 10^{-6}$  m, after which it decreases slightly. The CNR increased over most of the tested  $\delta/\mu$  ratios. The standard deviation over each image stack of both SNR and CNR increased with increasing  $\delta/\mu$  ratio (Fig. 2 (a)). The line profile plot (Fig. 2 (b)) further illustrates that higher  $\delta/\mu$  ratios resulted in strongly smoothed reconstructed CT data, thus making the identification of the feature boundaries difficult. **In contrast, enhanced feature boundaries were pronounced in the tomographic reconstructions of the phase-retrieved projections at low  $\delta/\mu$  ratios.**

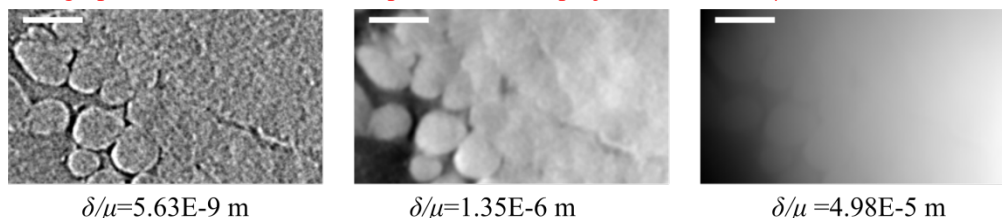


Fig. 3. Detail view of a tomographically reconstructed slice of a murine soleus muscle for various  $\delta/\mu$  ratios assessed by PPCI on a lab-based X-ray microscope. For increasing  $\delta/\mu$  ratios image blurring becomes dominant due to Paganin phase retrieval, which has low-pass filtering characteristics. For low  $\delta/\mu$  ratios, enhanced feature boundaries were observed due to X-ray interference, which is only weakly low-pass filtered during Paganin phase retrieval.  $\delta/\mu = 1.35 \times 10^{-6}$  m in-between these extremes provides visually good results. Scale bar =  $50 \mu\text{m}$ .

Figure 3 supports this observation, with reconstructed data at small  $\delta/\mu$  ratios showing prominently image noise and enhanced feature boundaries, whilst at large  $\delta/\mu$  ratios reconstructed data were smoothed such that internal structures of the muscle could not be recognised. An optimal ratio will lie in between these extremes.

As a compromise between maximal SNR and CNR on the one hand, and the described critical trade-off for image sharpness on the other hand, a  $\delta/\mu$  ratio of 1.35E-6 has been selected as the  $\delta/\mu$  ratio providing optimum image quality of the tomographic reconstructions from PPCI image data captured on a lab-based X-ray microscope and at an effective propagation distance of  $R_{III_{Lab}}$ .

The  $\delta/\mu$  ratios finally obtained for all effective propagation distances and imaging systems are summarised in Table 3.

**Table 3. Optimal  $\delta/\mu$  ratios for different experimental settings**

X-ray source	Position	Detector pixel size ( $\mu\text{m}$ )	$Z_{eff}$ (mm)	$\delta/\mu$ ratio (m)
Versa 510, Zeiss Xradia	$R_{I_{Lab}}$	6.72	8.57	1.35E-6
	$R_{II_{Lab}}$	6.72	17.14	1.35E-6
	$R_{III_{Lab}}$	6.72	34.29	1.35E-6
SLS, TOMCAT	$R_{I_{Syn}}$	0.65	~29.96	9.25E-7
	$R_{II_{Syn}}$	0.65	~39.94	9.25E-7
	$R_{III_{Syn}}$	0.65	~49.90	9.25E-7
	$R_{IV_{Syn}}$	0.65	~59.86	9.25E-7

### 3.2 Image quality vs. propagation distance and exposure time for lab-based X-ray microscope

Based on the previous result on image quality a  $\delta/\mu$  ratio of 1.35E-6 has been applied for all following experiments. Figure 4 (a) shows the SNR and CNR obtained for different effective propagation distances and exposure times (see Table 1) using the lab-based X-ray source. The tomographic reconstructions after phase retrieval yielded a relatively low average SNR and CNR for the lowest effective propagation distance of 8.57 mm ( $R_{I_{Lab}}$ ), namely  $1.95 \pm 0.16$  and  $1.75 \pm 0.21$ , respectively. Both SNR and CNR decreased for larger effective propagation distances at a non-adjusted exposure time of 5 sec (see Table 1), i.e. at  $R_{III_{Lab}}$  the SNR was  $0.95 \pm 0.22$  and the CNR  $1.00 \pm 0.21$ . For an adjusted exposure time however both SNR and CNR increased with increasing propagation distance, i.e., the SNR reached  $2.51 \pm 0.26$  and the CNR  $2.71 \pm 0.33$ . This difference of the SNR and CNR for different exposure times is due to lower X-ray fluxes and hence higher noise levels at larger distances, which can be compensated by increasing the exposure time. The reduction in image noise and increase in SNR and CNR is also emphasised when considering the line profiles shown in Figure 4 (b). Whilst for both non-adjusted and adjusted exposure times, the step height decreased with increasing effective propagation distance, the change in step height was lower for the adjusted exposure times.

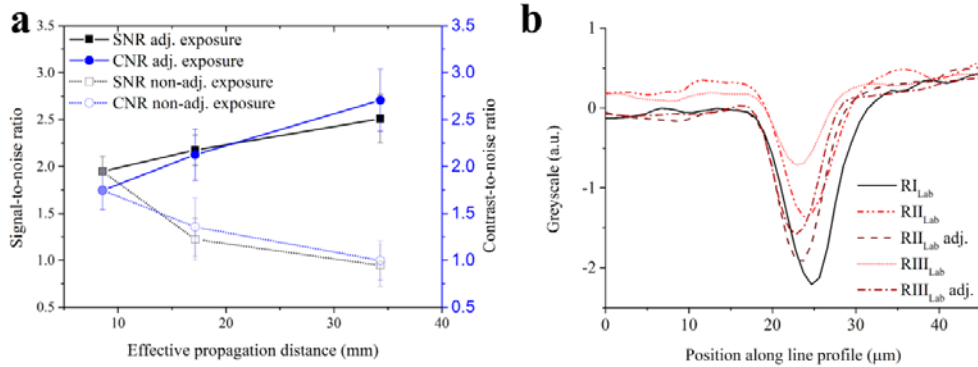


Fig. 4. Image quality from PPCI on a lab-based X-ray microscope for different propagation distances. (a) Signal-to-noise ratio (SNR) and contrast-to-noise ratio (CNR) of tomographic PPCI data for different effective propagation distances. Both SNR and CNR increased for larger X-ray propagation distances, where reduced X-ray flux loss has been adjusted by longer exposure times. (b) Line profiles over two feature boundaries within a tomographically reconstructed slice of a murine soleus muscle for different source-to-sample and sample-to-detector distances (positions RI<sub>Lab</sub>, RII<sub>Lab</sub> and RIII<sub>Lab</sub> in Table 1) assessed by PPCI for adjusted and non-adjusted exposure times.

### 3.3 Image quality improvement for lab-based X-ray microscope by application of Paganin phase retrieval

Figure 5 (a) and (b) shows the comparison of a tomographically reconstructed slice without and with prior Paganin phase retrieval for the lab-based X-ray microscope. Figure 5 further depicts the difference in (c) SNR and (d) CNR for tomographic reconstructions after Paganin phase retrieval (“Paganin phase retrieved”) and for tomographic reconstructions only (“Non-phase retrieved”). Application of Paganin phase retrieval led to an increase in tomographic image quality by more than one order of magnitude.

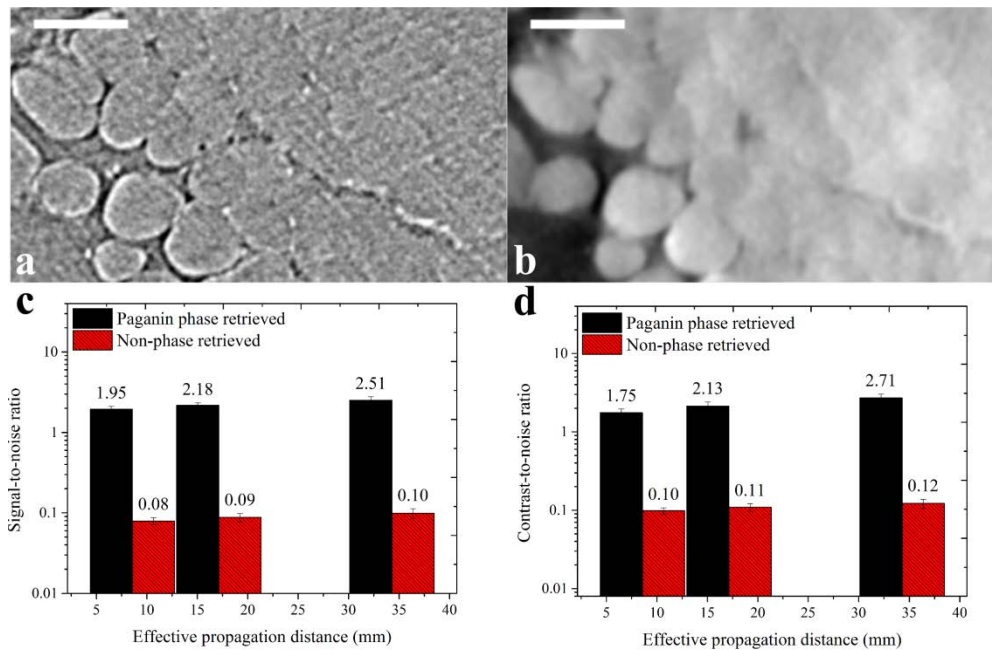


Fig. 5. Increase in image quality on a lab-based X-ray microscope due to Paganin phase retrieval. Tomographically reconstructed slice for image data (a) without and (b) with prior Paganin phase retrieval, respectively. (c) & (d)

Signal-to-noise ratio (SNR) and contrast-to-noise ratio (CNR) for tomographic data with (solid black) and without (shaded red) prior phase retrieval step. Phase retrieval improved the tomographic image quality by more than an order of magnitude. (a-d) Data shown is from a murine soleus muscle assessed by PPCI.

### 3.4 Image quality vs. propagation distances for synchrotron radiation source

Figure 6 (a) shows the SNR and CNR computed for different sample-to-detector distances ( $R_2 = 30$  mm, 40 mm, 50 mm and 60 mm) from tomographic PPCI data obtained using synchrotron radiation at the TOMCAT beamline of the SLS. The SNR decreased by 28% between  $R_2 = 30$  mm (SNR =  $72.3 \pm 0.3$ ) and  $R_2 = 60$  mm (SNR =  $52.0 \pm 0.2$ ). Similarly, The CNR values decreased from  $R_2 = 30$  mm (CNR =  $20.1 \pm 1.5$ ) to  $R_2 = 60$  mm (CNR =  $15.4 \pm 0.8$ ) by 23%.

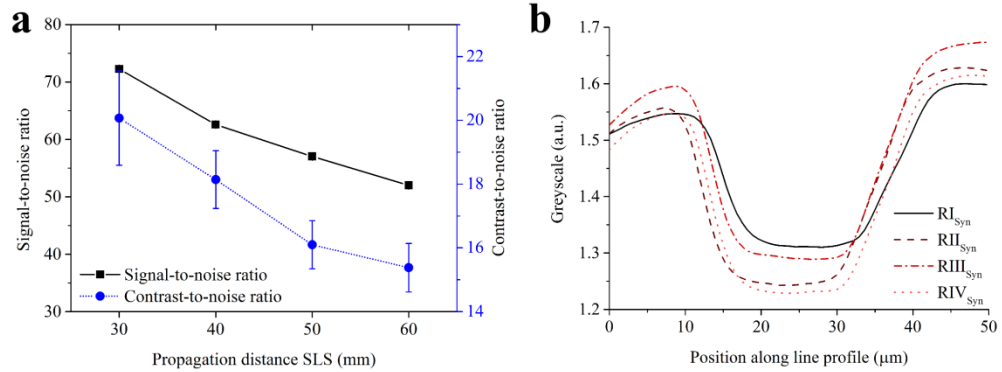


Fig. 6. Image quality after phase retrieval using  $\delta/\mu$  ratios as described in Table 3 at a synchrotron source for different (effective) propagation distances. (a) Signal-to-noise ratio or SNR (black solid line) and contrast-to-noise ratio or CNR (blue dashed line). (b) Line profiles over two feature boundaries within tomographic PPCI data (positions RI<sub>Syn</sub>, RII<sub>Syn</sub>, RIII<sub>Syn</sub> and RIV<sub>Syn</sub> in Table 1). Data acquired at TOMCAT beamline of the Swiss Light Source. SNR and CNR were generally high, but decreasing with larger (effective) propagation distances. Feature boundaries were pronounced to a higher extent for increasing (effective) propagation distances.

The line profiles shown in Figure 6 (b) however reflect a slight increase in image sharpness with increased (effective) propagation distance, as the feature boundary height became more pronounced.

### 3.5 Visibility of soft tissue features

Figure 7 shows a direct comparison between tomographic PPCI data of a murine soleus muscle obtained from the lab-based and synchrotron source. The comparison is made at different effective propagation distances for the lab-based system with adjusted exposure times ((a) RI<sub>Lab</sub>: 5 sec for  $Z_{eff} = 8.57$  mm, (b) RII<sub>Lab</sub>: 20 sec for  $Z_{eff} = 17.14$  mm and RIII<sub>Lab</sub>: 82 sec for  $Z_{eff} = 34.29$  mm) and synchrotron data at the largest propagation distance (RIV<sub>Syn</sub>: (d) 180 ms at  $R_2 = 60$  mm or  $Z_{eff} = 59.86$  mm). A nerve fibre is highlighted, which is clearly visible in the synchrotron data, but can also well be distinguished for RIII<sub>Lab</sub> in the lab-based data. However, for RI<sub>Lab</sub> and RII<sub>Lab</sub> on the lab-based system, it becomes more difficult to clearly identify nerve fibres and generally, to distinguish distinct tissue features.

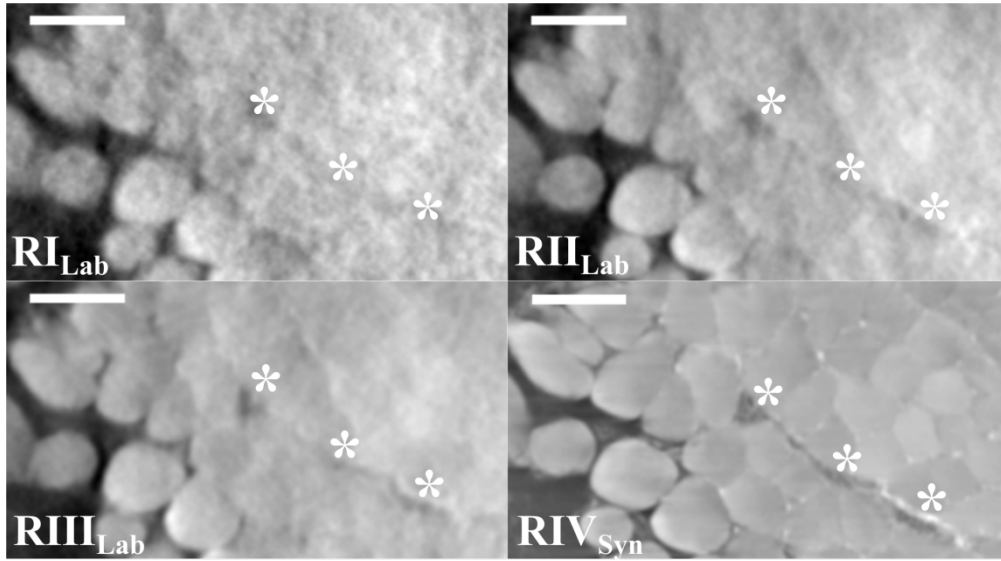


Figure 7: Comparison of lab-based and synchrotron-based tomographic PPCI of mouse soleus muscle. For the lab-based X-ray microscope tomographic data is shown for three different effective propagation distances (and adjusted exposure times) at position  $RI_{Lab}$  (exposure time = 5 sec,  $Z_{eff} = 8.57$  mm),  $RII_{Lab}$  (exposure time = 20 sec,  $Z_{eff} = 17.14$  mm) and  $RIII_{Lab}$  (exposure time = 82 sec,  $Z_{eff} = 34.29$  mm). Synchrotron-based data has been retrieved for position  $RIV_{Syn}$  (exposure time = 0.18 sec,  $R_2 = 60$  mm or  $Z_{eff} = 59.86$  mm). \* mark nerve fibres.

#### 4. Discussion and conclusions

The  $\delta/\mu$ -ratios stated in Table 3 do not agree with theoretical considerations. Namely, despite the increase in effective propagation distance we found the optimal  $\delta/\mu$ -ratio to remain constant for the three effective propagation distances investigated on the lab-based system. This may be explained by the image noise in the respective images, in particular for the lowest effective propagation distance  $RI_{Lab}$ . The adjustment for difference in detector pixel size for the change from lab-based system to the synchrotron led to a change from  $\delta/\mu = 1.35E-6$  m to  $\delta/\mu = 9.25E-7$  m. However, an increase in propagation distance again did not require a change in  $\delta/\mu$ -ratio. This is in contrast to the theory described by equation (5). On the other hand, Paganin phase retrieval may not be the most adequate phase retrieval algorithm for the applied imaging settings (see discussion below). It is however one of the most easily available algorithms and appears to result in images of good quality.

The increase in effective propagation distance improved the image quality in lab-based data sets for adjusted exposure times, which is in agreement with previous studies [10, 21, 22]. In particular, little tissue structure was visible at an effective propagation distance of 8.57 mm compared to well-defined structures and visibility of features such as nerves at 34.29 mm, which was reflected by a 1.5-fold increase in CNR. In the case of the non-adjusted exposure time an increase in effective propagation distance led to a decrease in both SNR and CNR, which is in agreement with the results published by Bidola *et al.* [16]. Namely, Bidola and co-workers concluded the best effective propagation distance to be 8.57 mm for the same lab-based  $\mu$ CT system and using comparable experimental settings [16]. However, these authors did not adjust the exposure time to account for the decrease in photon count with increasing effective propagation distance. The decrease in CNR in the present work was more than 40%, whereas Bidola *et al.* determined a decrease of less than 10% for what they define as SNR (which is  $CNR\sqrt{0.5}$ ) [16]. However, this difference may stem from the fact that Bidola *et al.* computed the SNR only for X-ray projections, but not for the reconstructed CT data. The line profiles further highlight the difference in image quality for adjusted and non-adjusted

exposure time and consistently, it is difficult to distinguish nervous tissue from muscle fibres for small effective propagation distances (especially for  $RI_{Lab}$  and to some extent for  $RII_{Lab}$ ). At the same time, longer exposure times lead also to longer scan times, with the adjusted exposure time of 82 seconds per frame resulting in a 36.5 hour CT scan, whereas the scan would have been completed within about 2 hours for a 5 second exposure time.

In the case of the synchrotron radiation-based data, SNR and CNR continuously decreased in the regions investigated for increasing effective propagation distances in a moderate fashion. This is in disagreement with findings by Kitchen *et al.* [21], where in the case of phase retrieved data and for any chosen exposure time the SNR increased with increasing propagation distance. In the non-retrieved data, the SNR decreased with increasing propagation distance [21]. The (fixed) choice of  $\delta/\mu$  in [21] thus appears to have been such that the resulting smoothing reversed the relationship between SNR and propagation distance. In this work, in contrast to [21], the  $\delta/\mu$  ratio was chosen with respect to optimal sharpness as well as SNR and CNR. In addition to computing the CNR for the image contrast between general muscle tissue and background only, one could also compute a second CNR between muscle fibres and nerve fibres to determine the image quality in terms of internal tissue contrast. A more general method to characterise image quality may be to compute the SNR in the Fourier space instead of real space, thus avoiding the limitation to specific ROIs and obtaining a measure of quality independent of the application of Fourier filtering.

The applied Paganin filter acts as a low-pass filter, thus reducing the image noise and facilitating the identification of soft tissue features. The gain  $G$  in SNR by moving from attenuation contrast to phase contrast was defined by Kitchen *et al.* as  $G = SNR_{phase}/SNR_{attenuation}$  [21]. The authors found that  $G$  increases both with increasing propagation distance and decreasing exposure time, thus allowing for a steep reduction of radiation dose [21]. In the present experiment, we find that the gain increased from  $G = 24.6$  for  $RI_{Lab}$  to  $G = 28.0$  for  $RII_{Lab}$  in the case of a non-adjusted exposure time and to  $G = 25.4$  for  $RIII_{Lab}$  for an adjusted exposure time. However, Kitchen and colleagues did not account for a change in feature visibility, i.e. sharpness, which is known to decrease for smaller Fresnel numbers and thus larger propagation distances [19]. Depending on the size of the feature of interest, this must be accounted for. Furthermore, whilst the gain in SNR was higher for the non-adjusted exposure time, the feature visibility was poor, due to the larger image noise (see Figure 7). It would be interesting to investigate how much of the increase in gain is due to smoothing by the Paganin filter alone, thus by comparison with the smoothing that can be achieved by applying a Gaussian filter or an edge-preserving filter for instance. Furthermore, taking into account the Fresnel number  $F$  and the validity of the near field approximation ( $F \gg 1$ ), it may be beneficial to consider the use of other phase retrieval algorithms as  $F = 0.16$  for  $RI_{Syn}$  and  $F = 0.08$  for  $RIV_{Syn}$  (for  $RI_{Lab}$   $F = 51$  and  $RIII_{Lab}$   $F = 13$ ). The contrast transfer function can therefore no longer be approximated as being linear [23] and the assumptions, on which the transport of intensity equation is based, no longer hold [19]. Other phase retrieval algorithms can then be employed (although other approximations may still apply), such as extended contrast transfer functions-based methods [24-27] or algorithms based on Born- or Rytov-type approximations [28], as discussed in [1, 29].

Nonetheless, despite the violation of the near field condition, the images obtained at the synchrotron source were of better image quality than those obtained on a lab-based system. Namely, SNR and CNR in the case of adjusted exposure times for the lab-based X-ray microscope are one order of magnitude below that of the synchrotron at a similar distance (and significantly lower exposure time). Similarly, the image quality in directly reconstructed data sets (no phase retrieval) was lower in the lab-based data sets by one order of magnitude at similar  $Z_{eff}$  (data not shown here), i.e.  $SNR = 0.099 \pm 0.014$  for  $RIII_{Lab}$  vs.  $0.943 \pm 0.005$  for  $RI_{Syn}$ , respectively. The difference in X-ray flux between synchrotron and lab-based system

thus remains one of the main obstacles for imaging of soft tissues on lab-based machines when relying on X-ray absorption.

From the  $\delta/\mu$  sweep it followed that the optimal ratio to be used for phase retrieval was  $\delta/\mu = 1.35\text{E-}6$  m in this specific example of a paraffin wax-embedded muscle. This value is compromise between the global image quality metrics SNR, CNR and sharpness. The optimal ratio is around 240 times larger than that for water and almost 100 times larger than that for paraffin wax (see Table 2). This study highlights the importance of the chosen  $\delta/\mu$ -ratio, which stands in contrast to Kitchen and co-workers noting that Paganin phase retrieval is quite insensitive to variations of this ratio [21]. **The optimal  $\delta/\mu$ -ratio was determined for each propagation distance but was found to be constant for each imaging setting. This is in contrast to what would be expected from equation (5) in the Appendix.** Thus, in the case of Kitchen *et al.*, the  $\delta/\mu$  ratio of water worked well for larger distances, but would be considered non-optimal for smaller distances [21]. **Therefore, the  $\delta/\mu$ -ratio should be adapted to the given application, having in mind the specific image processing and segmentation approaches involved.**

Overall, we have shown that lab-based systems can be used to identify microscopic soft tissue features, such as nerves, in mouse muscle using appropriate effective propagation distances, exposure times and phase retrieval settings. The image quality is generally lower than at synchrotron sources but lab-based X-ray microscopes can provide SNR and CNR levels that are comparable to synchrotron results, sufficient for identification of microscopic features in soft tissues. Imaging on a lab-based X-ray microscope at comparable SNR and CNR levels is however associated with much higher scanning times (several hours instead of minutes only). Depending on the feature of interest it may be possible for lab-based X-ray systems to lower the propagation distance and imaging time further, whilst still obtaining all structural information needed for specific applications.

## Funding

The authors would like to acknowledge funding by the Engineering and Physical Sciences Research Council (EPSRC) for the EPSRC doctoral training grant of author B. Zeller-Plumhoff and the British Heart Foundation for grant PG/12/18/29453. Furthermore, author B. Zeller-Plumhoff acknowledges funding by the German Federal Ministry of Education and Research (BMBF) for grant 05K16CGB.

## Acknowledgements

The authors would like to thank Matthieu Boone and Jelle Vlassenbroeck for the in-depth and fruitful discussions on the Octopus Imaging Software. Thanks also to Julian Moosmann for the discussions regarding phase retrieval algorithms. The synchrotron radiation data of the mouse muscles was obtained at the TOMCAT beamline of the Swiss Light Source (SLS). We acknowledge the Paul Scherrer Institut, Villigen, Switzerland for provision of synchrotron radiation beamtime at the TOMCAT beamline of the SLS. We further acknowledge support by the  $\mu$ -VIS X-ray Imaging Centre at the University of Southampton for using the ZEISS Xradia Versa 510 system and image processing and analysis tools. Thanks to Charalambos Rossides for his thorough proofreading.

## 5. Appendix

### 5.1 Effective energy

For the polychromatic source of the lab-based X-ray microscope the effective energy had to be determined, upon which the X-ray absorption and scattering of materials depend (and thus  $\delta/\mu$ ). To this end, a 0.54 mm thin (measured by calliper) polytetrafluoroethylene ( $\text{H}_2\text{F}_4$ ) sheet (PTFE Sheet 0.5 mm; Bearing Boys Ltd, Norfolk, UK) that is weakly absorbing X-rays has

been used as phantom according to the procedure described by Bidola *et al.* [16] at 40 keV (X-ray tube potential peak) and a tube power of 3 W. Briefly, the projected thickness of the phantom can be calculated by an approximation of the transport-of-intensity equation for a point-source illumination [13] by

$$t(x, y) = -\frac{1}{\mu} \ln \left( \mathbf{F}^{-1} \left\{ \frac{\mathbf{F} \{I / I_0(x, y)\}}{1 + \frac{\delta}{\mu} Z_{eff} (u^2 + v^2)} \right\} \right), \quad (5)$$

where  $I_0$  is the intensity of the incident X-ray beam (flat field image without object in X-ray path) and  $I$  the intensity of the X-ray beam (X-ray projection with object in X-ray path) that are recorded on the detector,  $Z_{eff}$  the effective propagation distance (see below),  $\delta$  and  $\beta$  the decrement of the real part and the imaginary part of the refractive index (with linear attenuation coefficient  $\mu = 4\pi/\lambda \cdot \beta$ ), respectively, and  $\lambda$  the wavelength.  $F$  and  $F^{-1}$  are the forward and inverse Fourier transforms and  $(x, y)$  the spatial variables, with  $(u, v)$  the corresponding spatial frequencies. Assuming a density of  $2.2 \text{ g/cm}^3$ ,  $\delta$  and  $\mu$  have been retrieved from the X-ray Database from the Center for X-Ray Optics at the Lawrence Berkeley National Laboratory's Materials Sciences Division (<http://henke.lbl.gov>, accessed 27-September-2017) [20]. The appropriate effective energy has been determined by plotting the projected thickness of the PTFE phantom for different energies (11.0 keV, 12.2 keV, 13.0 keV, 14.0 keV) around 13.0 keV (Fig. 8), which is the approximate effective energy at 40 keV peak voltage of the same source according to Bidola *et al.* [16]. At an energy of 12.2 keV the projected thickness matched the measured PTFE thickness of 0.54 mm and thus, has been selected as the effective energy used for phase retrieval here.

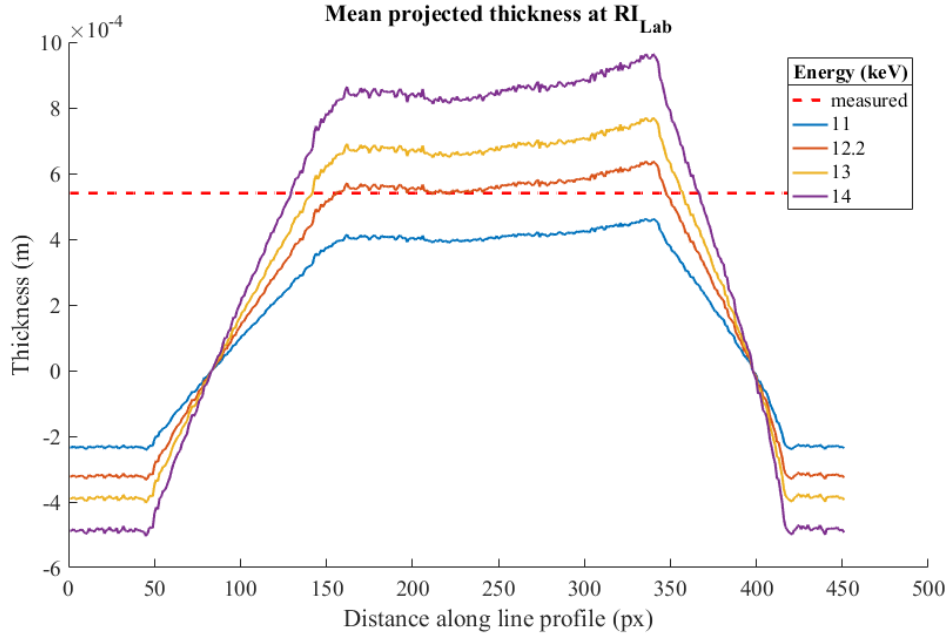


Figure 8: Line profiles over the projected thickness of the phantom. The red dashed line represents the measured thickness of the phantom ( $\text{H}_2\text{F}_4$  sheet). The projected thickness was computed via equation (5) at  $\text{RI}_{\text{Lab}}$  (effective propagation distance of 8.57 mm). The best match of projected and measured thickness was found for 12.2 keV.

## 5.2 Testing of $\delta/\mu$ -ratios for other distances

We used Paganin phase retrieval to retrieve the data for different  $\delta/\mu$ -ratios around the ratio  $1.35\text{E-}6$  which was optimal for  $\text{RIII}_{\text{Lab}}$ . As previously described, both SNR and CNR were computed, along with line profiles assessed across edges. Figure 9 shows the line profiles for  $\text{RI}_{\text{Lab}}$ ,  $\text{RII}_{\text{Lab}}$  and  $\text{RIII}_{\text{Lab}}$  for three different  $\delta/\mu$ -ratios. It appears that the ratio at  $1.35\text{E-}6$  is the optimal value for all distances, as the edges became smoother for larger distances, whilst the SNR and CNR still increased (Fig. 10). Similarly, Figure 11 shows the line profiles across edges for  $\text{RI}_{\text{Syn}}$  and  $\text{RIV}_{\text{Syn}}$  which appear to differ only insignificantly for each  $\delta/\mu$ -ratio tested. Therefore, the same ratio of  $9.25\text{E-}7$  was used for phase retrieval, where edges were still well-defined but some smoothing had occurred. The SNR for  $\text{RI}_{\text{Syn}}$  stayed significantly above that for  $\text{RIV}_{\text{Syn}}$  (Fig. 12), whilst the CNR increased strongly for the lower effective propagation distance and increasing  $\delta/\mu$ -ratio, and to a lesser extent for the larger effective propagation distance.

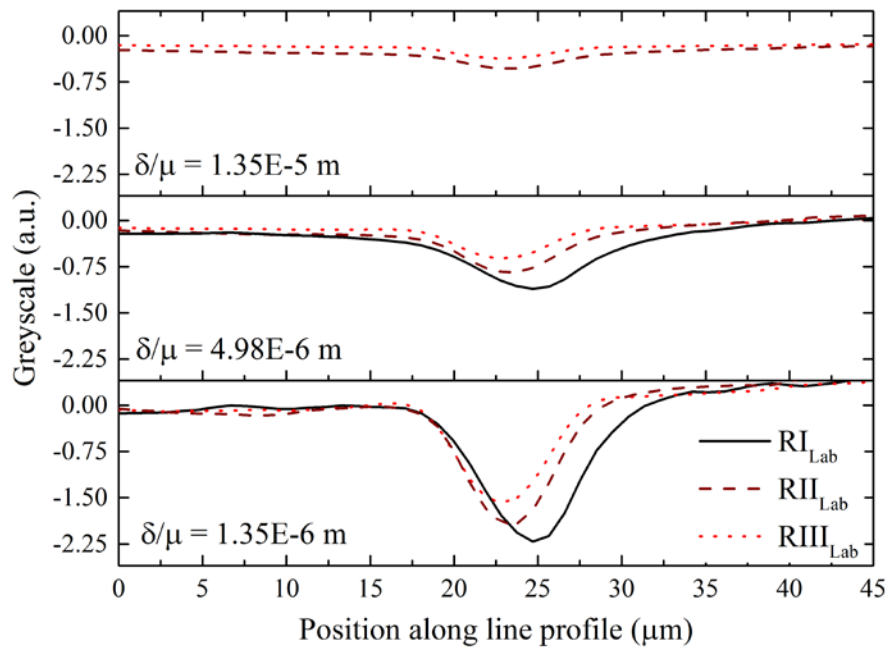


Figure 9: Line profiles computed over two edges for the lab-based system at all three effective propagation distances (with adjusted exposure times) and for three different  $\delta/\mu$ -ratios. An increase in the selected  $\delta/\mu$ -ratio resulted in a strong smoothing of the edge and the  $\delta/\mu$ -ratio of  $1.35\text{E-}6$  was determined best for all three effective propagation distances.

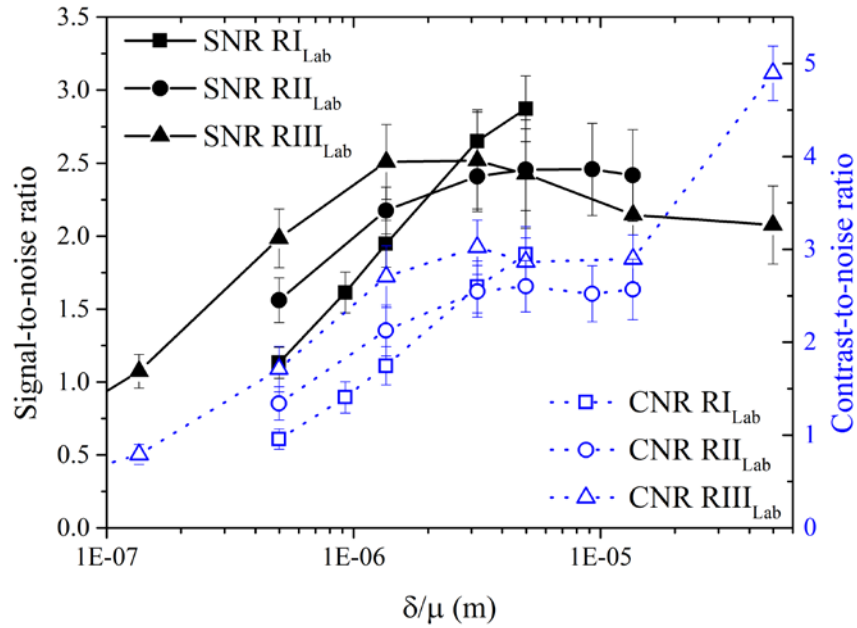


Figure 10: Signal-to-noise ratio and contrast-to-noise ratio for the lab-based system at the three different effective propagation distances (with adjusted exposure time) and for different  $\delta/\mu$ -ratios. Generally, both SNR and CNR increased for larger  $\delta/\mu$ -ratios, yet a plateau was reached beyond a certain point.

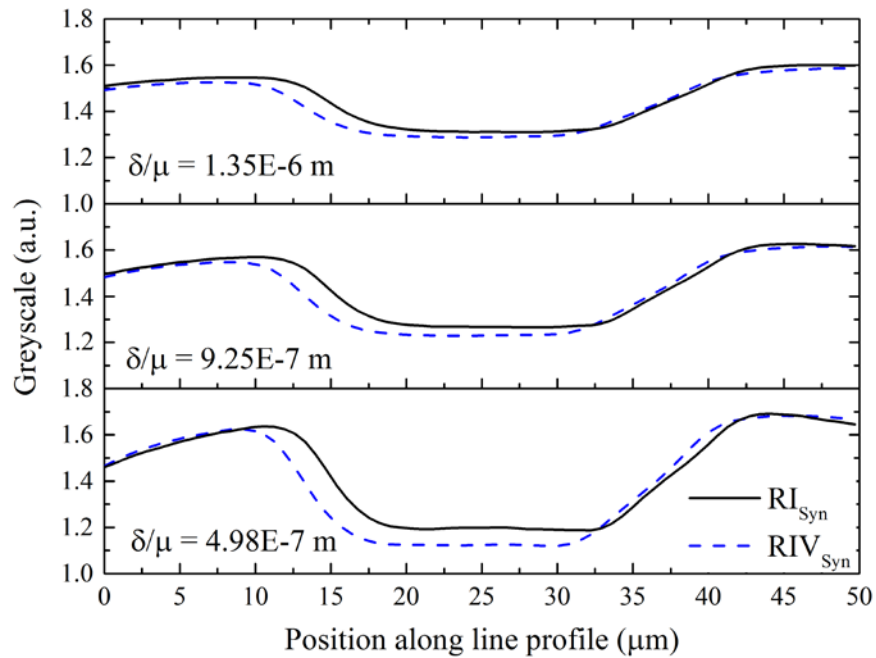


Figure 11: Line profiles computed over two edges for the synchrotron case at the smallest and largest effective propagation distance ( $RI_{Syn}$  and  $RIV_{Syn}$ , respectively) and for three different  $\delta/\mu$ -ratios. An increase in the  $\delta/\mu$ -ratio resulted in a smoothing of the edges. The ratio of  $9.25E-7$  was determined best for all effective propagation distances.

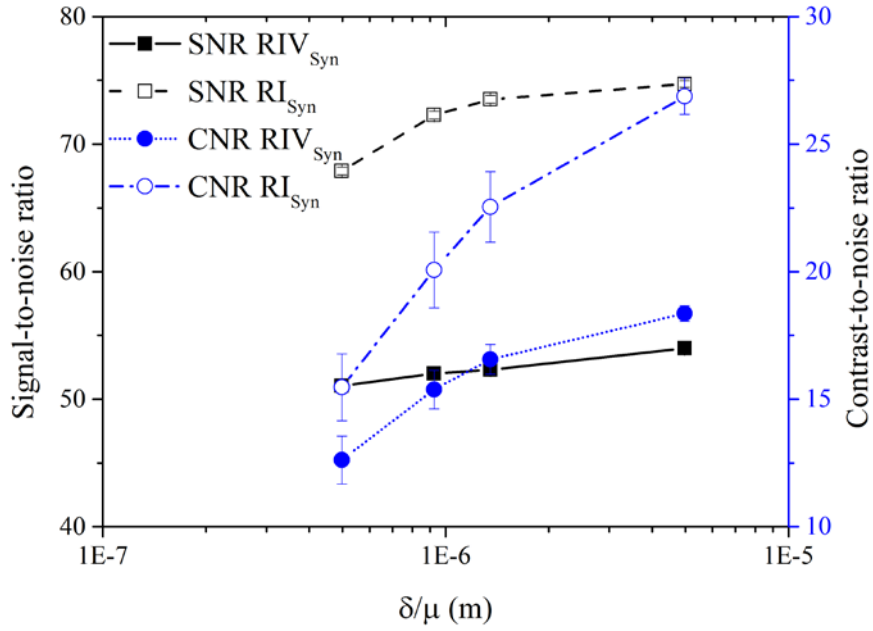


Figure 12: Signal-to-noise ratio and contrast-to-noise ratio for the synchrotron case at the smallest and largest effective propagation distance ( $RI_{Syn}$  and  $RIV_{Syn}$ , respectively). The SNR for  $RI_{Syn}$  stayed significantly above that for  $RIV_{Syn}$ , whilst the CNR increased strongly for the lower effective propagation distance and increasing  $\delta/\mu$ -ratio, and to a lesser extent for the larger effective propagation distance.